Free-standing 100 nm Period Gratings Produced by Achromatic Holographic Lithography

by

Satyen N. Shah

S.B., Massachusetts Institute of Technology (1993)

Submitted to the Department of Electrical Engineering and Computer Science
in partial fulfillment of the requirements for the degree of

Master of Engineering in Electrical Engineering and Computer Science

at the

MASSACHUSETTS INSTITUTE OF TECHNOLOGY

February 1995

Author ....
Department of Electrical Engineering and Computer Science
February 3, 1995

Certified by ....
Henry I. Smith
Joseph F. and Nancy P. Keithley Professor of Electrical Engineering
Thesis Supervisor

Accepted by ....
Frederic R. Morgenthaler
Chairman, Department Committee on Graduate Theses

Free-standing 100 nm Period Gratings Produced by Achromatic Holographic Lithography

by

Satyen N. Shah

Submitted to the Department of Electrical Engineering and Computer Science
on February 3, 1995, in partial fulfillment of the
requirements for the degree of
Master of Engineering in Electrical Engineering and Computer Science

Abstract

In this thesis, I refined and improved an implementation of achromatic holographic lithography (AHL), a method of producing fine period gratings over large areas. As a specific application, I attempted to produced large area free-standing gratings, which are in demand for atomic-beam interferometry research. This thesis describes the improvements I made to the implementation of AHL at the Nanostructures Laboratory at MIT as well as the process of fabricating large area free-standing $100nm$ period gratings.

Thesis Supervisor: Henry I. Smith
Title: Joseph F. and Nancy P. Keithley Professor of Electrical Engineering

Acknowledgments

First, I wish to thank my advisor, Professor Hank Smith, for giving me the opportunity work in his group. His insistence on following the scientific method was probably the most difficult and most important lesson I had to learn at M.I.T. I also wish to thank my academic advisor, Professor Jeffrey Shapiro, for his guidance in my academic pursuits.

I began my work at the Nanostructures Lab very green and accident-prone and owe thanks to the lab staff for their expertise and their patience. I am grateful to Jim Carter for demonstrating how to get things done quickly and forcefully, and to Mark Mondol for his help and humor. I thank Jeanne Porter and Bob Sisson for teaching me most of the lab procedures I know. My gratitude goes to Rich Aucoin for his unselfish support. I acknowledge Michael Weinberg for his speedy and efficient administration.

My time at NSL has given me the opportunity to work alongside Martin Burkhardt, Dave Carter, Juan Ferrera, Nitin Gupta, Scott Hector, Jim Hugunin, Keith Jackson, Hui Ying Lee, Julie Lew, Mike Lim, Euclid Moon, Tom Murphy, Gabrielle Owen, Irv Plotnik, Scott Silverman, Vince Wong, Isabel Yang, and Ken Yee. They all share a place in my memories of the lab.

My heartfelt thanks go to my parents for their love and encouragement and for giving me this rich education.

I wish success to Tim Savas and Dr. Mark Schattenburg in continuing the research on this project.

Contents

List of Figures

Chapter 1

Introduction

There is currently a demand for structures with periods in the $50 - 100nm$ range. These structures will find application as UV polarizers, quantum-effect electronics, fiducial references, and UV and X-ray spectroscopy tools. In particular, free-standing gratings will aid atomic-beam interferometry research [1].

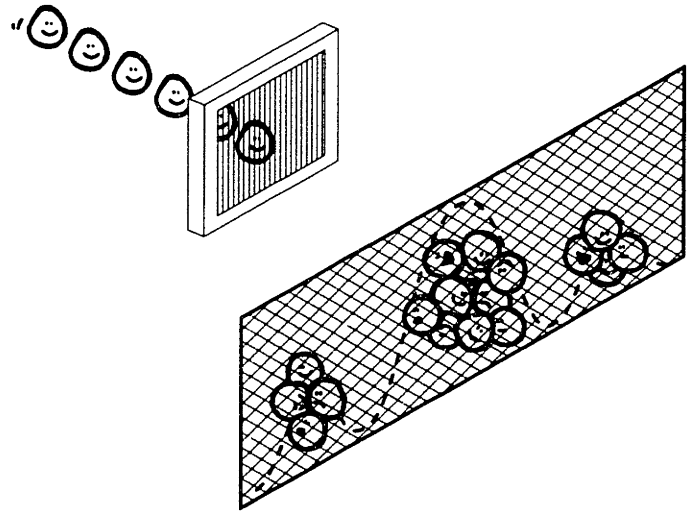

Figure 1-1: An atomic beam demonstrates interference after passing through a free-standing grating.

The goal of AHL is to produce such structures. There are a variety of methods for artificially producing fine period structures today. They include electron beam lithography, focused ion beam lithography, and coherent holographic lithography. However, while electron and ion beam lithography are suitable for writing arbitrary patterns, their times

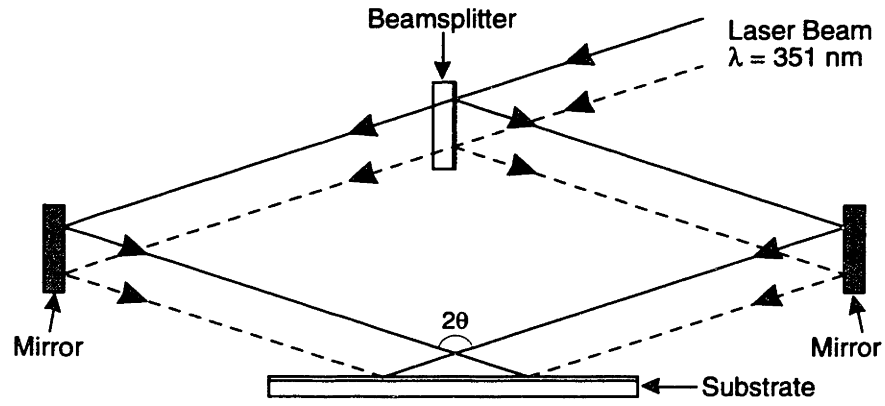

Figure 1-2: Coherent holographic lithography images a standing wave with period $P = \lambda/2 \sin\theta$ over a large area. The shortest available period is $135nm$ using a frequency doubled Ar ion laser.

for writing large-area gratings are prohibitively long. Moreover, they cannot by themselves achiece long-range spatial-phase coherence. Thus for writing large-area fine-period gratings, coherent holographic lithography is the preferred alternative.

Coherent holographic lithography is a method of imaging a standing wave created by a highly coherent source as in Figure 1-2. Such lithography requires a highly coherent light source with wavelength λ, and the finest grating period it can produce is $\lambda/2$. The lack of powerful, highly coherent laser sources with wavelengths shorter than $257nm$ makes coherent holographic lithography unable to produce grating periods shorter than about $135nm$ over a substantial area.

To move past this barrier A. Yen at the Submicron Structures Lab at MIT developed Achromatic Holographic Lithography to create gratings with periods down to $100nm$ [2]. This method requires using only a partially coherent laser source with $\lambda < 200nm$ and a pair of large-area, high-quality parent gratings with $P = 200nm$. The technology for creating such parent gratings was available within the Submicron Structures Lab.

Figure 1-3 presents a simple summary how AHL works. The key feature to derive from the figure is that by doing holographic lithography with gratings instead of mirrors, one can image a large-area fine-period grating without using a source that features high spatial and temporal coherence. Figure 1-4 illustrates the implementation of AHL at the Nanostructures Lab at MIT.

Chapter 2 of this thesis describes a significant change to the white-light interferometer

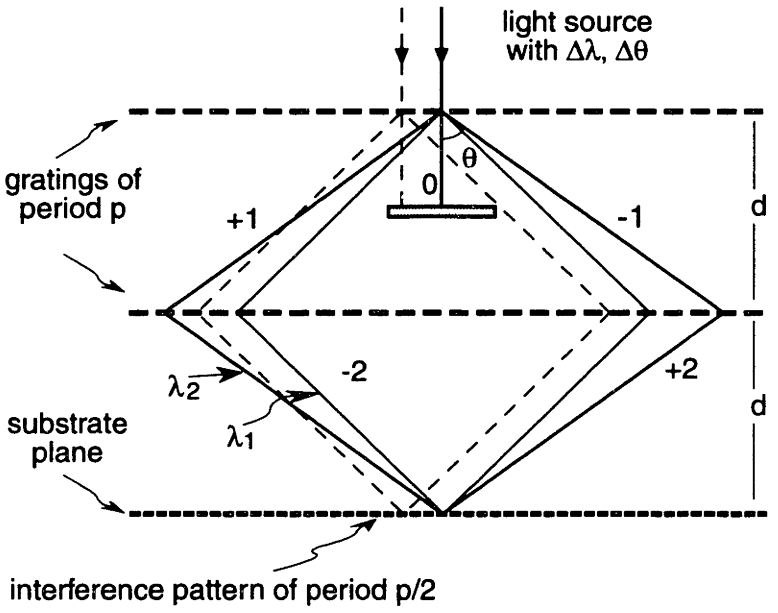

Figure 1-3: The essence of Achromatic Holgraphic Lithography. For each point on the beamsplitter grating there is a conjugate point on the substrate.

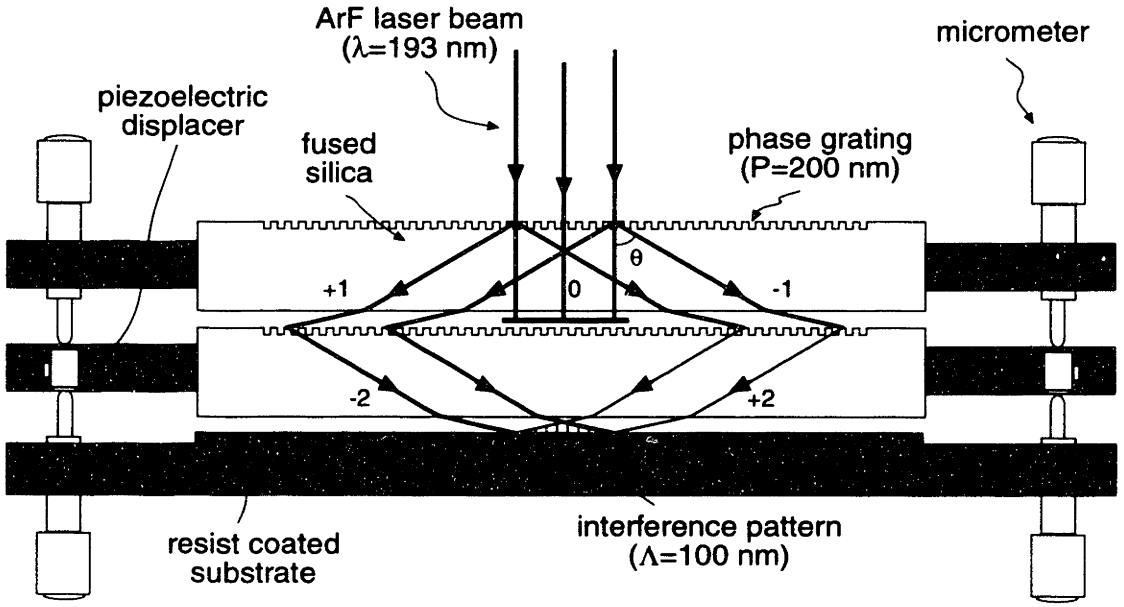

Figure 1-4: Cross-section of the AHL setup at NSL at MIT. The beam-splitter and recombiner phase gratings, both having a $200nm$ period, are permanently etched in identical quartz discs. A. Yen used holographic lithography to make the phase gratings and tuned the grating profiles to maximize the efficiency of the desired diffracted orders.

for setting equal gaps [3]. The improved interferometer enables more precise alignment of the substrate in the focal plane, a requirement for high-contrast grating exposure.

Chapter 3 lists several other improvements to the AHL system which I made over the course of my research. These include improved alignment procedures, improvements for increasing the area of the gratings, and the evolution towards a more robust AHL system.

Chapter 4 describes further study of A. Yen's anti-reflection (ARC) coating for $\lambda = 193nm$. This ARC layer sits beneath the PMMA resist layer, and is necessary for attenuating reflections from the substrate. These reflections would otherwise wash out the contrast.

Chapter 5 of this thesis outlines the processing of free-standing $100nm$ period gratings. Previous research at MIT has produced $200nm$ period free-standing gratings [4] and has proposed $100nm$ period free-standing gratings [5]. This chapter describes a first attempt at producing such gratings. Figure 1-5 shows a rough outline of the additional processing for producing free-standing gratings.

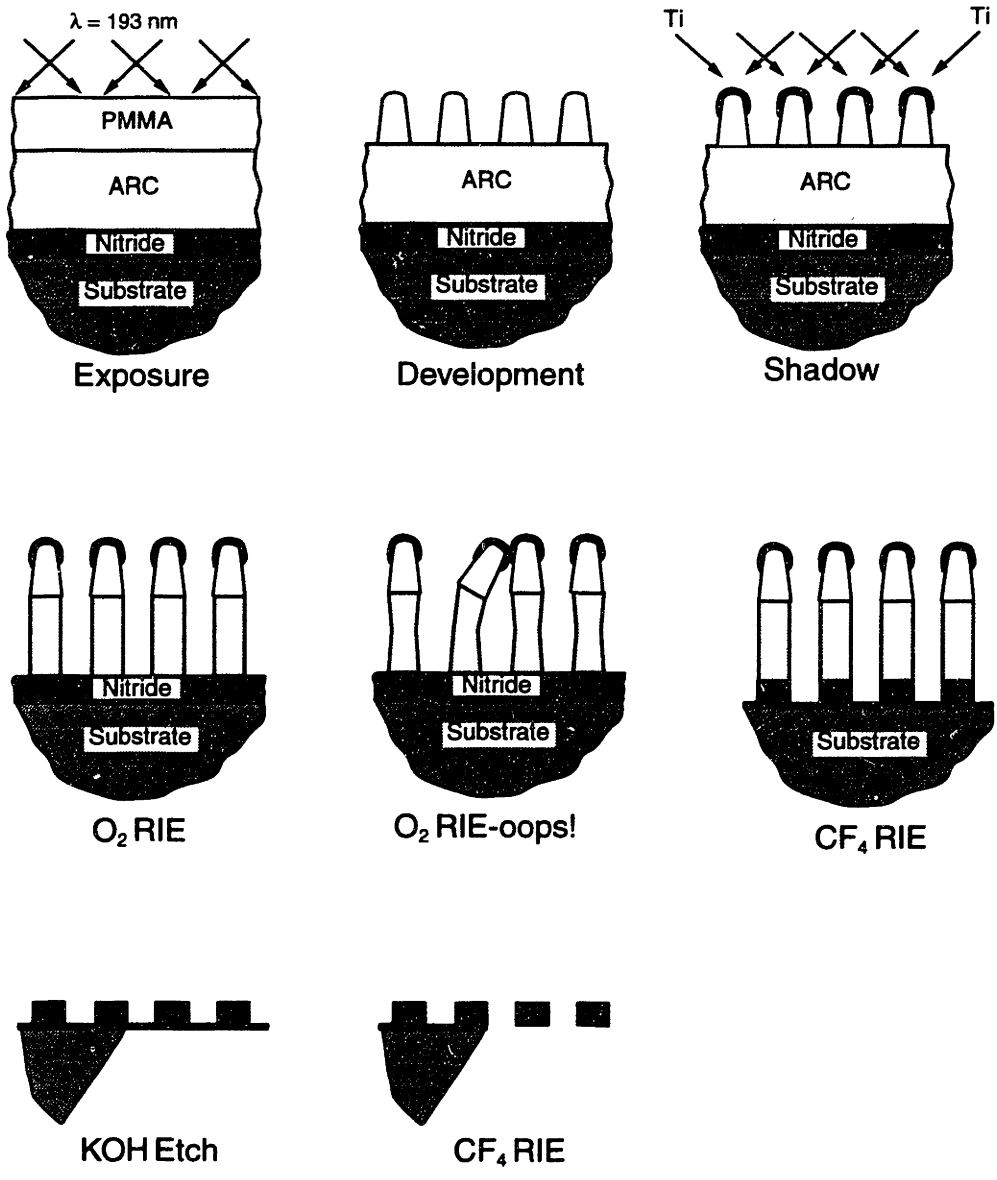

Figure 1-5: Generalized process for making free-standing gratings. This 2D view does not illustrate the additional processing necessary for creating the support structures.

Chapter 2

The White-Light Interferometer for Setting Equal Gaps

In my previous thesis, I gave an incorrect value of the sensitivity of the white-light interferometer used for setting equal gaps. Recall that for high-contrast gratings, the substrate must lie within a depth of focus Δd given by

$$\Delta d = \frac{\sqrt{p^2 - \lambda^2}}{2\Delta\theta} \tag{2.1}$$

where p is the period of the parent gratings, λ is the wavelength of the laser source, and $\Delta\theta$ is the angular divergence of the laser beam. In our setup $p = 200nm$, $\lambda = 193nm$, and $\Delta\theta$ is up to 6 milliradians. These values yield a depth of focus budget of approximately $10\mu m$. However, working underbudget yields a bonus of higher contrast.

For an interferometer at an angle θ as in Figure 2-1a, the relationship of g, the displacement of the substrate required to shift the intensity at the output, B, by 1 radian, and θ is $g = 2\lambda/\sin\theta$, not $g = 2\lambda\sin\theta$ as I previously stated. The derivation of this expression is located in Appendix A.

This result shows that the interferometer is most sensitive when θ is maximum. The tradeoff of higher θ is lower fringe contrast at the output, B. However, using a lock-in amplifier combined with piezoelectric displacers and a sensitive photodetector, there is in fact adequate signal in the interferometer in Figure 2-1b with $\theta = 90^o$. Figure 2-2 illustrates the setup neccesary for detecting the signal.

An advantage of using $\theta = 90^o$ instead of $\theta = 11^o$ is that the geometry of the old setup in

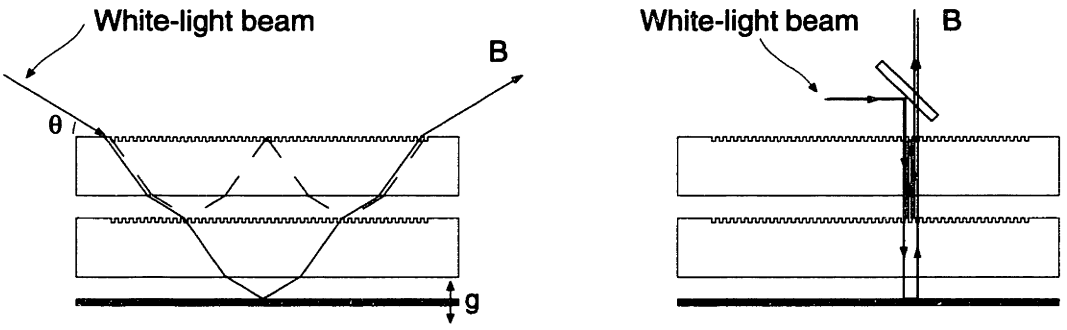

Figure 2-1: The old and new paths in the white-light interferometer. The interferometer on the left is more accurate, and the interferometer on the right is more precise.

Figure 2-1a restricts the region of the substrate which the interferometer sees. The setup in 2-1b makes it posssible for one to position the interferometer on any region of the substrate instead of only the center of the substrate.

The tradeoff with using the new setup is that the paths of the white-light beams no longer closely match the paths of the excimer beam, so this new interferometer helps only when the surfaces of the two quartz flats are parallel and flat, and more significantly, when the difference in optical thickness of the flats is less than the depth of focus. Since a Michelson interferometer verified that the difference in thickness of the quartz plates is less than $0.5\mu m$, this drawback is tolerable.

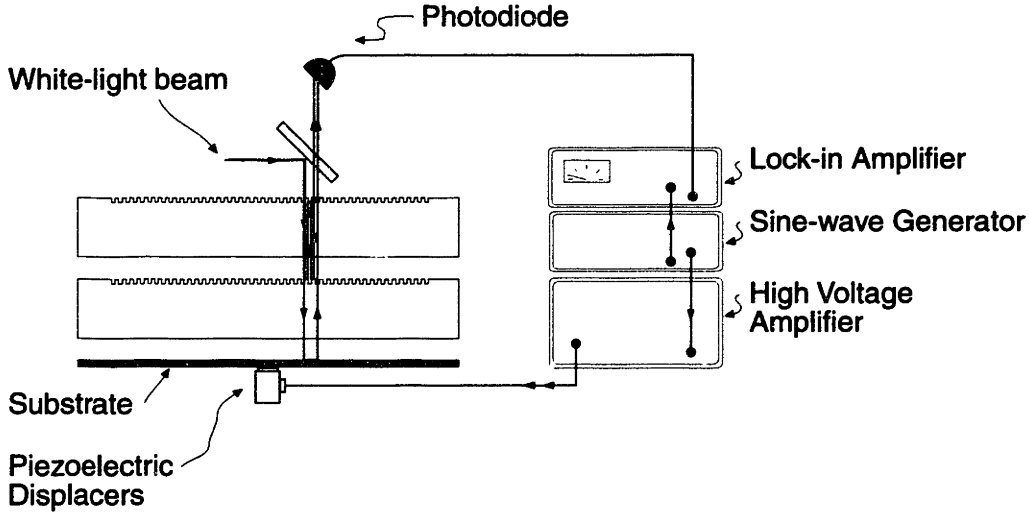

Figure 2-2: Setup of the white-light interferometer. The lock-in amplifier filters the noise from the weak signal.

Chapter 3

Improvements to the Apparatus

3.1 Fixtures

In the AHL apparatus, the "recombiner" grating is rigidly attached to the optical table. Separate fixtures hold the "beamsplitter" grating in front and the vacuum pinchuck for the substrate in back. In the original apparatus, the mechanical spacers (such as Scotch tape and optical fiber) for setting equal gaps provided mechanical stability, and exposure times were short so vibration was not a great concern. However, substituting the white-light interferometer for mechanical spacers in the setup resulted in fixtures that are free to sway and defocus the substrate during exposure. Longer exposure times for larger area gratings amplify this problem.

For better rigidity, the new apparatus has three contact points around the circumference of the beamsplitter grating and the substrate. At these points, springs pull the fixtures together and micrometers space them apart, allowing one to adjust the two gaps. In order to very precisely vary the gap size without varying the gap parallelism, the micrometers on the substrate fixture bear against three piezoelectric stacks driven by a common high-voltage source [6]. Variations among the three piezos is not a concern since the hysteresis of the piezos is generally much smaller than the flatness of the substrate.

An extra micrometer at the base of the beamsplitter fixture adjusts the parallelism of the beamsplitter grating with respect to the recombiner grating.

After taking a number of exposures yielding low contrast and distortion (Figure 3-3), we determined that the phase gratings or the substrate may be rotating during the exposure. Our solution was to attach sheets of spring steel to the apparatus to prevent parts of the

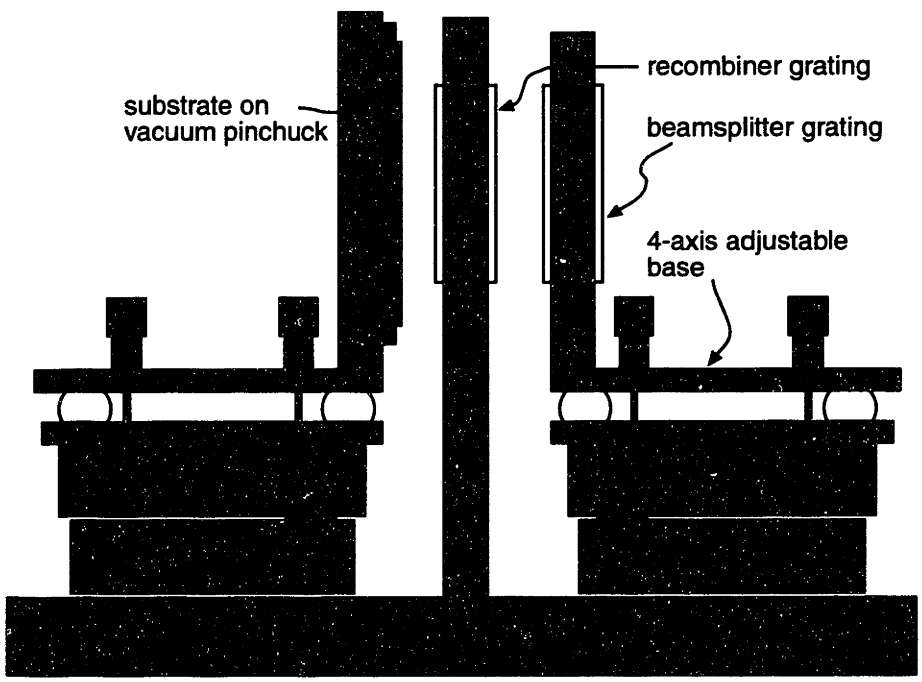

Figure 3-1: Drawing of the original AHL system. Originally there were mechanical spacers such as Scotch tape and optical fiber in the gaps. The substitution of the white-light interferometer for such spacers makes the system less rigid.

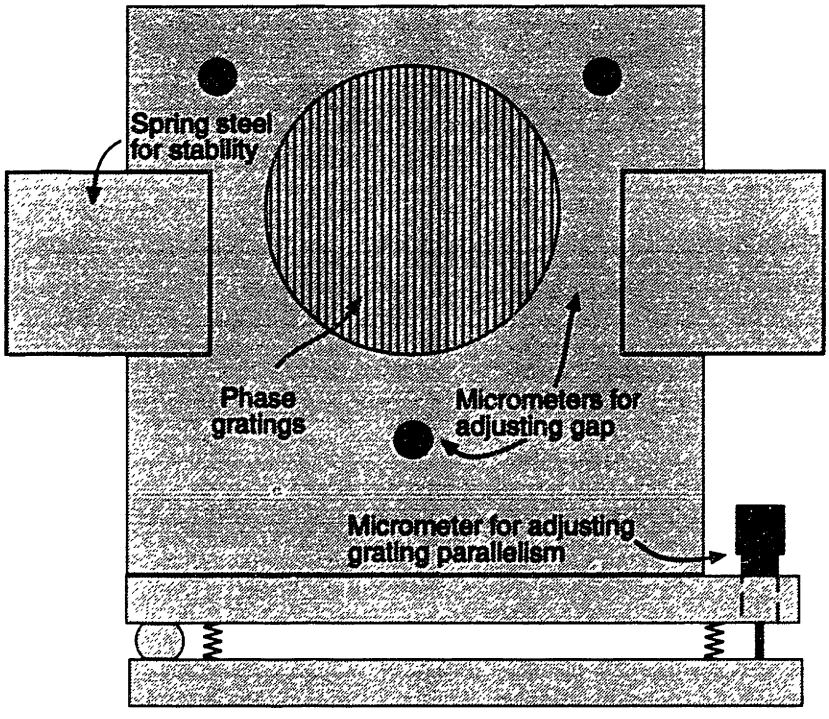

Figure 3-2: Front view of the new fixture for holding the beamsplitter grating. The fixture for holding the substrate does not feature the rotational adjustment, but does feature piezoelectric displacers for precise gap adjustment.

apparatus from shifting laterally or from rotating during exposure. Figure 3-2 illustrates how the apparatus incorporates these stabilizers.

3.2 Beam Scanning

The attractive feature of AHL is its ability to write gratings over large areas, so it important to exploit this.

By scanning the beamsteering optics in a direction perpendicular to the gratings, one can expose larger areas. The previous setup used a DC motor and worm drive to scan the laser beam. DC motors exhibit unacceptable velocity ripple, however, which caused banding over the scanned area. We replaced it with a synchronous AC motor, model Bodine 2419 [7], and observed significantly less banding.

The width of the zero order stop limits the width of the scan. The amount of fan-out of the first-order diffracted beams limits the width of the zero order stop. The zero-order stop

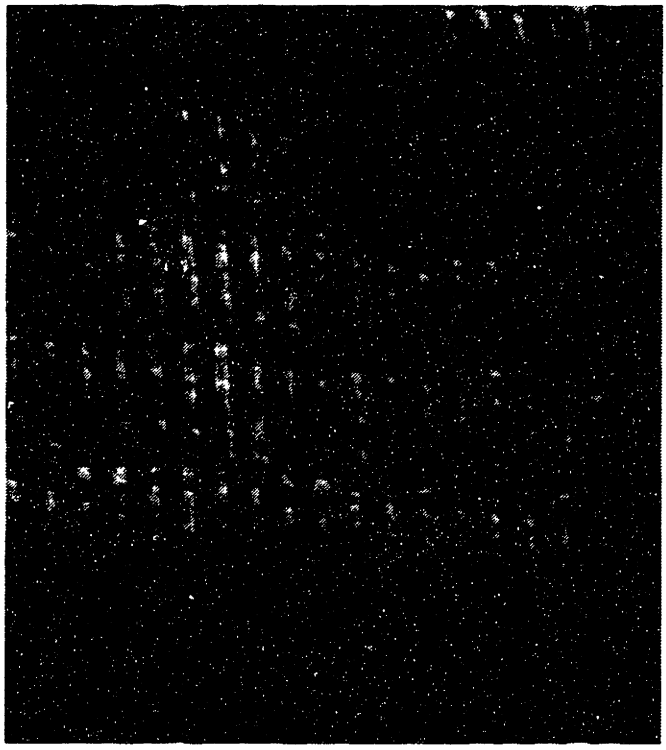

Figure 3-3: Spatial phase distortions in 100nm period gratings resulting from vibration during exposure. The steel sheets in the previous figure eliminate the distortion.

now in place is made of 0.5" wide, 0.001" thick ribbon steel stock. This material is thinner and less susceptible to creasing than the aluminum foil in the original setup. In the ArF laser beam this material exhibits discoloration but no ablation.

If the zero-order stop scans along with the beam, then the scannable area is limited only by the distance between the ± 1 orders reaching the substrate, which in this setup is about $3cm$. To perform this task an STS cable links the zero-order stop and the motor stage [8].

For larger areas, there must be two additional stops scanning in the substrate gap to allow only the ± 2 orders to reach the substrate. With these stops present, the area of writable grating is then limited only by the area of the phase gratings. With the current set of phase gratings, it is the recombiner grating that limits the maximum writable area.

3.3 Laser Collimation

On the Lumonics laser, the beam profile diverges originating at a point approximately $60cm$ behind the laser aperture. Beam divergence perpendicular to the gratings is undesirable as it lowers grating contrast. Beam divergence parallel to the gratings is desirable; it makes the beam profile uniform over a larger area. To optimize this situation, the system uses a cylindrical lens to collimate the beam [9]. The lens' focal point is $60cm$ behind the laser aperture and its axis is parallel to the gratings. The lens has dielectric coatings for $\lambda = 193nm$, and its focal length is $96cm$. Traditional alignment of a collimating lens involves using an optical wedge. However, the optical thickness of the wedge must be less than the coherence length of the laser beam, and such a wedge ($40\mu m$ thick) is not readily available. An alternate mothod of aligning the lens is by time-reversing the beam.

The first step of this technique is inserting a slit aperture in front of the laser and parallel to the phase gratings. Second, one inserts a dielectric-coated mirror in the path, and aligns it so that the ArF laser beam reflects back at the slit. Third, one places the cylindrical lens, mounted in a rotational stage on a post, in the beam path. The lens' height and rotation are properly aligned when the beam returns to the slit.

3.4 Characterization of Phase Gratings

With the existing set of phase gratings, I was unable to produce exposures highly uniform over an area more than $2mm$ across. Striking evidence of this problem appears in Figure

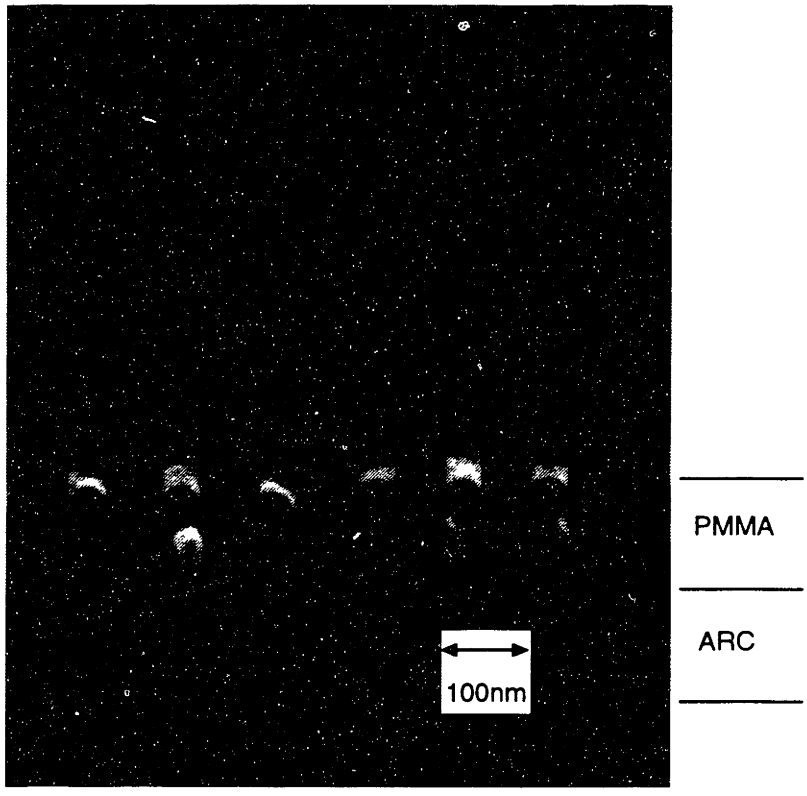

Figure 3-4: Best region of grating.

3-4 and Figure 3-4 showing SEM micrographs $3mm$ from each other on the same substrate. Since there is a synchronous motor sweeping the beam across the area several times during the exposure, the observation suggests variations exist over the area of the phase gratings. Indeed, the best region of the recombiner grating is its center even though the lithography images its edges.

Figure 3-6 is a plot of the efficiency of the 2nd difffracted order of the recombiner grating. This plot shows that the efficiency varies greatly (1.5-2.0% per millimeter) moving away from the center of the grating. This suggests changing linewidth or blazing (i.e. assymetrical grating profiles) near the edges of the recombiner grating (Figure 3-7). These are a result of the lithography and processing technology available to A. Yen for creating these phase gratings. Since that time research at MIT's Center for Space Research has yielded better lithography and processing technology, so grating uniformity should improve with forthcoming sets of phase gratings.

In addition, there are numerous scratches and defects on the existing phase gratings.

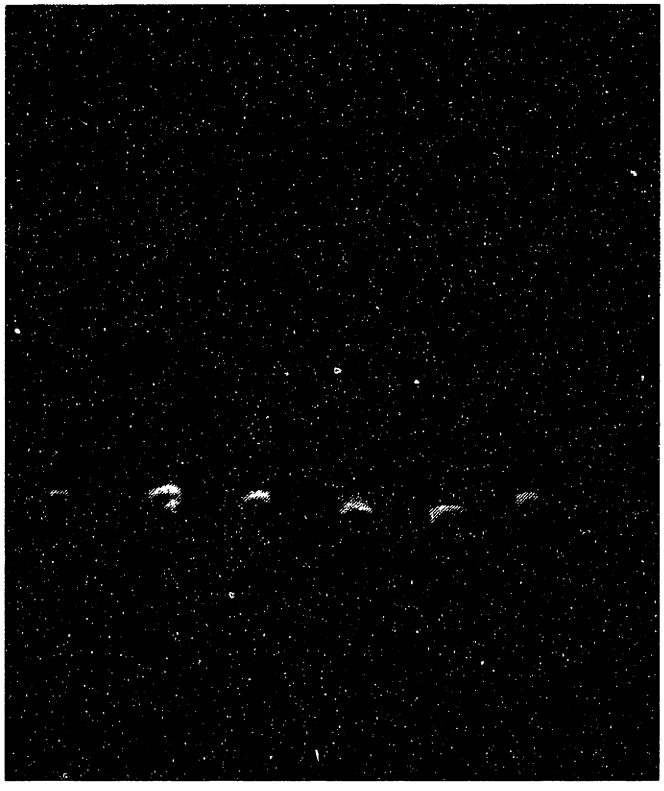

Figure 3-5: Same grating 3 mm away.

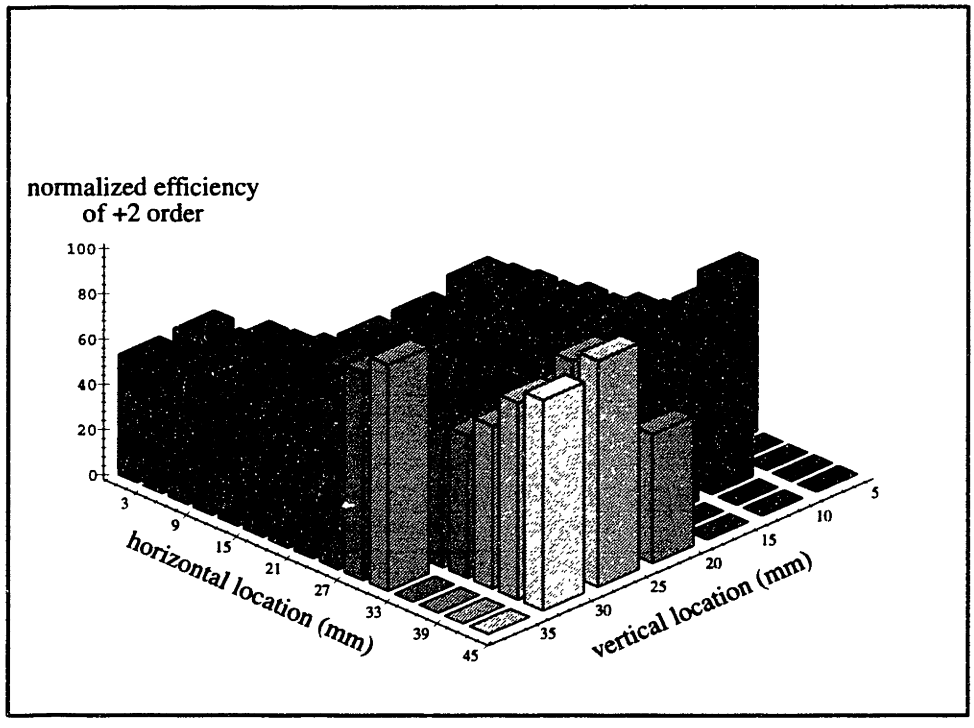

Figure 3-6: Plot of the efficiency of the +2 diffracted beam from the recombiner grating. Units on the vertical axis are normalized. The higher efficiency going to the right suggests nonuniform grating profiles.

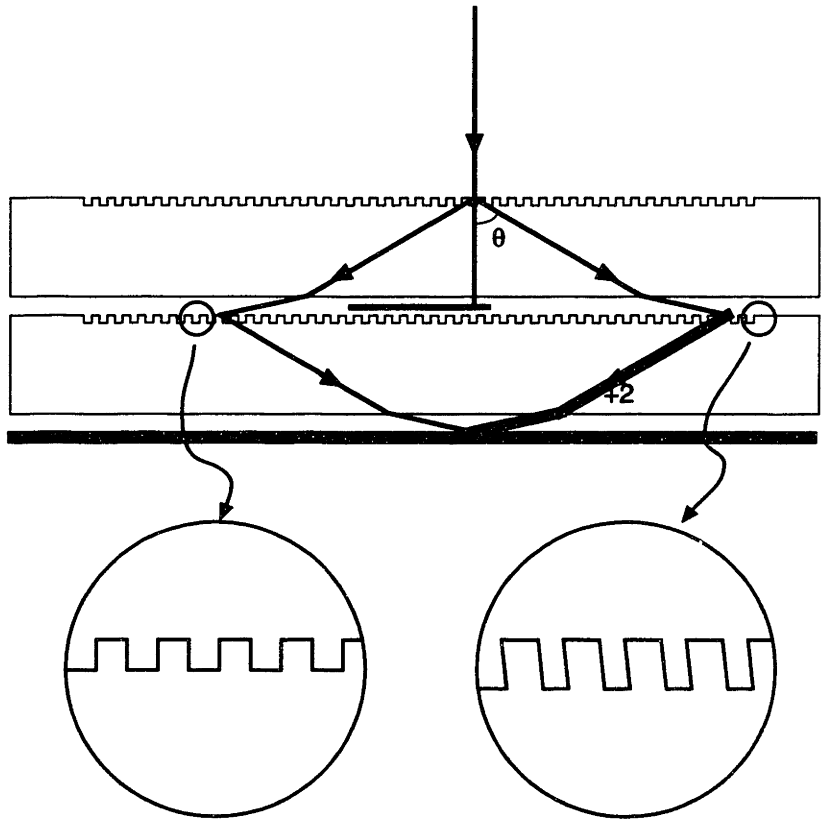

Figure 3-7: Changing phase-grating profiles affect the diffraction efficiency and hence lower the constrast and the uniformity of the lithography.

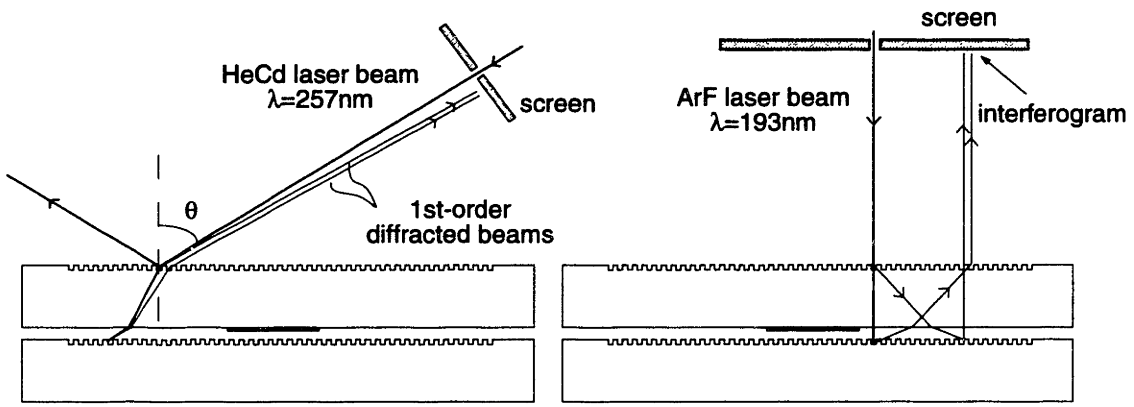

Figure 3-8: Two methods for achieving parallel phase gratings.

These blemishes are likely the result of repeated handling and are further incentive to generate a new set of gratings.

3.5 Achieving Parallel Phase Gratings

In his thesis, A. Yen presents two methods for aligning the phase gratings to sit parallel to one other. One method requires a HeCd laser ($\lambda = 325nm$), and the other requires the ArF laser itself. Figure 3-8 gives diagrams of the two alignment methods. Figure 3-9 is what a user sees during each alignment.

With a HeCd laser, three rows of spots converge. When they overlap, the gratings are parallel. For the best possible alignment the screen must be as far as possible from the gratings.

Using the ArF laser, one places a small aperture in the beam path, and then adjusts the grating parallelism until the rows of spots converge and a fringe pattern comes to view. Fine alignment requires use of a larger aperture (Figure 3-9(b)). The two stripes approximately $13mm$ from the aperture will demonstrate a specific fringe pattern.

Interpretation of the fringe pattern observed in the ArF laser beam remains a mystery. The pattern is different on the left and right sides of the aperture. The pattern does not sweep with beam, so the fringes are definitely an artifact present in the phase gratings, not in the laser source or beam-steering optics. The pattern is not highly sensitive to the parallelim of the gaps, though as the gaps lose parallelism, the fringes lose contrast.

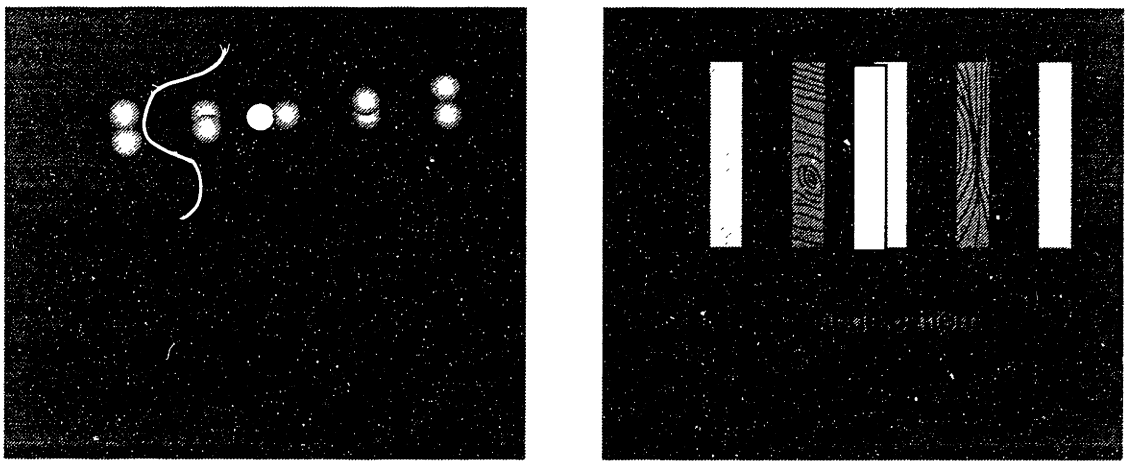

Figure 3-9: Back-diffracted HeCd and excimer laser beams for setting parallel phase gratings. Figure (a) represents misalignment using the HeCd, and Figure (b) represents best alignment using the excimer.

I suspect that the fringe pattern is an image of distortion in the phase gratings. It is interesting to note that at $\lambda = 193nm$, 1 fringe corresponds to only a $97nm$ difference in path length.

The ArF alignment method is preferable to the HeCd method. Because one is looking for a specific fringe pattern when using the ArF alignment, one has a more sensitive ($< 0.2mrad$ vs. $< 1mrad$) alignment than using the HeCd beam to get two spots to line up by eye. The HeCd laser is also cumbersome and occupies a large amount of real estate on the table.

Chapter 4

Study of Anti-Reflection Coating

4.1 Preparation of ARC

An anti-reflection coating (ARC) is necessary between the resist, composed of poly-methyl methacrylate (PMMA) and the silicon substrate because otherwise the severe index mismatch between the two would wash out the grating contrast. The ARC is a mixture of 4,4'-diazidodiphenyl sulfone (DDS or *bis*-azide) and PMMA. The function of the DDS is twofold, to cross-link the PMMA and to strongly absorb the $193nm$ wavelength. Using computer modeling, A. Yen devised an optimal 10:7 PMMA:DDS recipe, but eventually concocted a 4:3 PMMA:DDS recipe for experimental procedures because of uncertainties with measuring the mass of the PMMA. He used chunks of PMMA leached in-house from a solution, and powdered DDS and cyclopentanone, each bought from a vendor [10]. After mixing the ARC solution, the *bis*-azide does not dissolve completely, and before spin-coating one must filter the ARC through a syringe with $0.2\mu m$ pore filter.

Instead of mixing the ARC from scratch I ordered a 4% PMMA solution from a vendor [11]. According to the vendor, 950K PMMA in cyclopentanone is too large to pass through $0.2\mu m$ filter. This poses a problem since after adding the DDS, one must filter the ARC to $0.2\mu m$ to evenly spin-coat a 1400Å thick layer. If one uses a $0.45\mu m$ filter instead, undissolved particles in the ARC will cause streaks to appear after spinning. To work around this problem, one can dissolve the DDS separately in cyclopentatone and filter this solution to $0.2\mu m$ before adding it to the PMMA solution. Complete dissolution of the DDS requires spinning for two or more days at 30^oC. Because of the changes in the experimental procedure for mixing the ARC and the questions posed by the vendor about

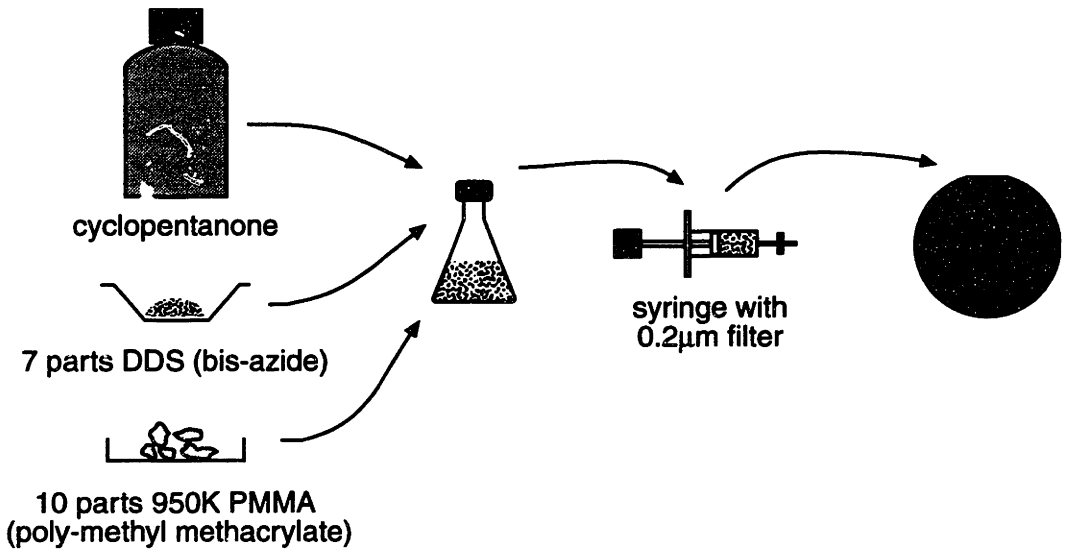

filtering PMMA, it is prudent to examine and reoptimize the recipe to ensure we use the optimal ARC blend and thickness.

4.2 Reformulation of ARC

Because the ARC consists solely of PMMA ($n \approx 1.68 + i0.0$) and DDS ($n \approx 1.3 + i0.75$), and the resist is PMMA, there is an inherent reflection at the resist-ARC interface. The ideal ARC would have low etch resistance and have an index nearly equal to that of PMMA (e.g. $n \approx 1.66 + i0.25$), This is possible by adding or substituting additional dyes and polymers in the ARC recipe. However, formulating the chemistry for a new resist is beyond the scope of this thesis.

Optimization of A. Yen's ARC recipe amounts to optimization of two variables: the absorber:PMMA ratio and the coating thickness. For this analysis I assume a thick absorber layer i.e., absorber thicknesses beyond which the energy reflected from the substrate accounts for less than 0.25% the total energy exposing the resist.

For a given contrast value/target, one can generally use a thinner ARC layer by adding more absorber to the ARC, but this comes at at cost of higher reflectivity at the resist-ARC interface. If one can afford to increase the thickness of the ARC, then the ARC can contain less absorber, and this lowers the reflection at the resist-ARC interface. Figure 4-1 illustrates this tradeoff.

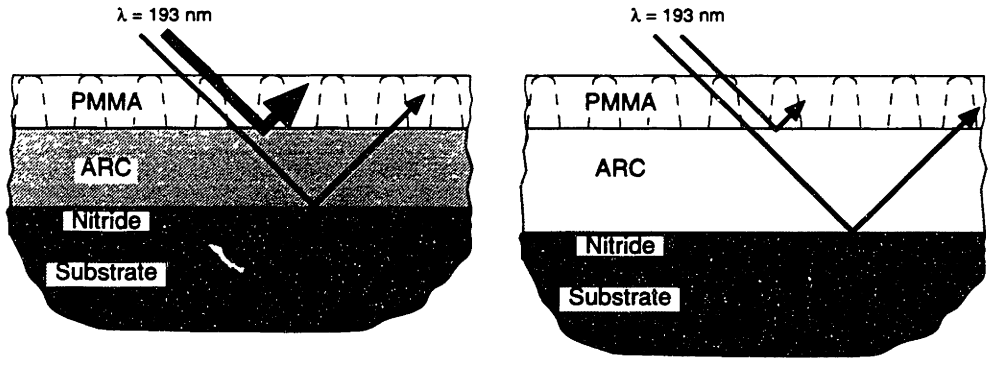

Figure 4-1: By darkening the ARC, the layer can be thinner, but the reflection at the interface worsens. By lightening the ARC, the reflection at the interface lowers, but one must etch through a thicker ARC.

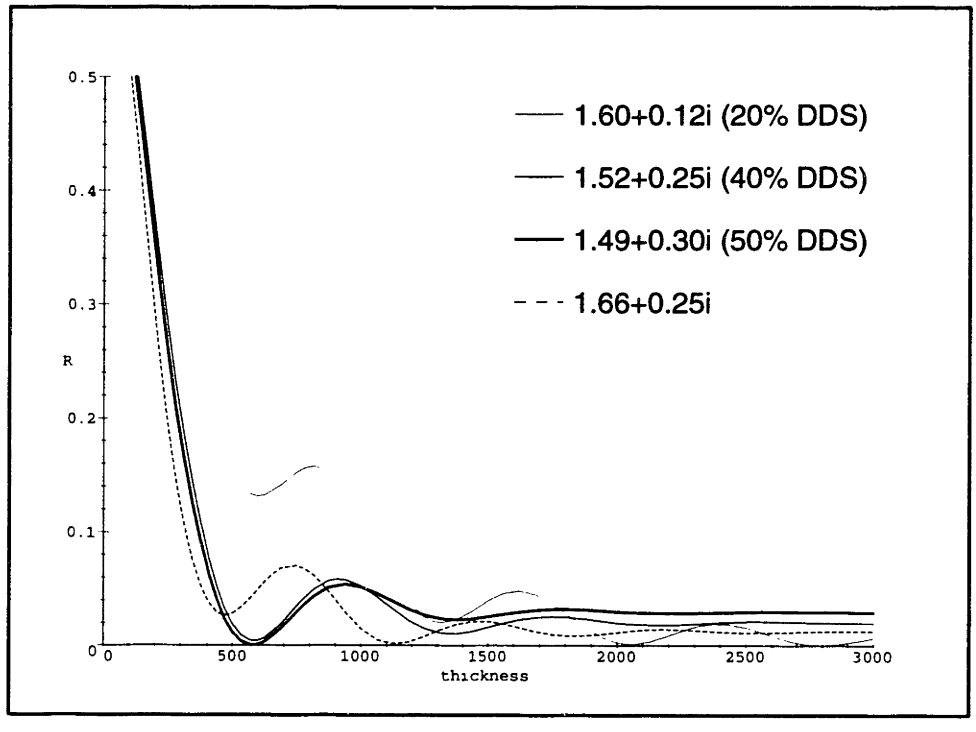

Figure 4-2: Relectivity at the resist-ARC interface for varying ARC indices and thicknesses (in Angstroms). The equations which generate these plots are in A. Yen's thesis. The dashed plot assumes a chemistry unavailable with PMMA and DDS alone.

The curves in Figure 4-2 represent indices available from different PMMA:DDS ratios. The plots assume that the index of the ARC is proportional to the concentration of DDS, and that ARC containing 40% DDS has index $n = 1.52+0.25i$. Note that these plots assume a silicon substrate, though in practice, we use silicon wafers for monitors, and silicon nitride wafers for actual processing. Future research will have to account for the indices of different substrates.

Therefore, in optimizing the ARC, one must consider two issues: First, how thick can the ARC become without stressing the processing technology. Second, what is the available contrast budget in the AHL.

I followed A. Yen's investigation of the ARC using an excimer laser to measure the reflectivity off the ARC at various angles to determine the ARC's real and imaginary indices. I was unable to measure the indices within ± 0.2 because of severe fluctuations in the power of the excimer beam.

Monitoring the development of grating samples I observed development rate was slower in the base of the PMMA layer (near the interface) than in the top of the PMMA, resulting in gratings that look underdeveloped. This suggests the dose is lower in the base of the PMMA, which implies that during the holography there is an orthogonal standing wave present in the PMMA with a node at the interface. This is a symptom of a poor index match at the ARC interface, i.e. there is too much absorber in the ARC. By changing the ARC recipe from 10 parts PMMA to 13 parts PMMA I was able to fix the grating profile.

With rigorous measurement techniques, the ARC could be used in the thin film regime i.e. at thicknesses where the reflection from the substrate destructively interferes with the reflection at the interface. An ellipsometer is now available that can measure complex indices down to $\lambda = 190nm$. This will enable better characterization of the ARC. In addition, such equipment will allow exploration of new ARC chemistries with a better matched resist-ARC interface.

Chapter 5

Procedure for Fabricating Free-standing Gratings

5.1 Purpose

The aim of this processing is to produce a free-standing grating for atomic-beam interferometry research in the lab of Professor Peter Töennies at the Max Planck Institute in Göttingen, Germany. Our specification is that the grating must be at least $10mm$ tall and $10\mu m$ wide. Such gratings would be unique since focused ion-beam lithography, which has produced 100 nm period free-standing gratings in the past, is unable to write a grating this large. The grating must sit on a platelet no larger than $8mm$ square. Figure 5-1 shows the design of the platelet.

5.2 Substrates

This procedure very closely follows the procedure in J. Lew's thesis. The substrates I used were a box of MEMC brand 3" wafers with a 1100Å layer of low-stress silicon-rich nitride, made in-house. Double-polished wafers are preferable though not necessary since the unpolished side will contain very large features. Note that the parameters I give work specifically for the box of nitride wafers I used. Since wafer thickness varies from box to box, and etch rates are difficult control, one must utilize extensive monitoring to continually adapt run parameters.

Prior to holographic exposure one must spin-coat the front side of the wafers with 1400Å

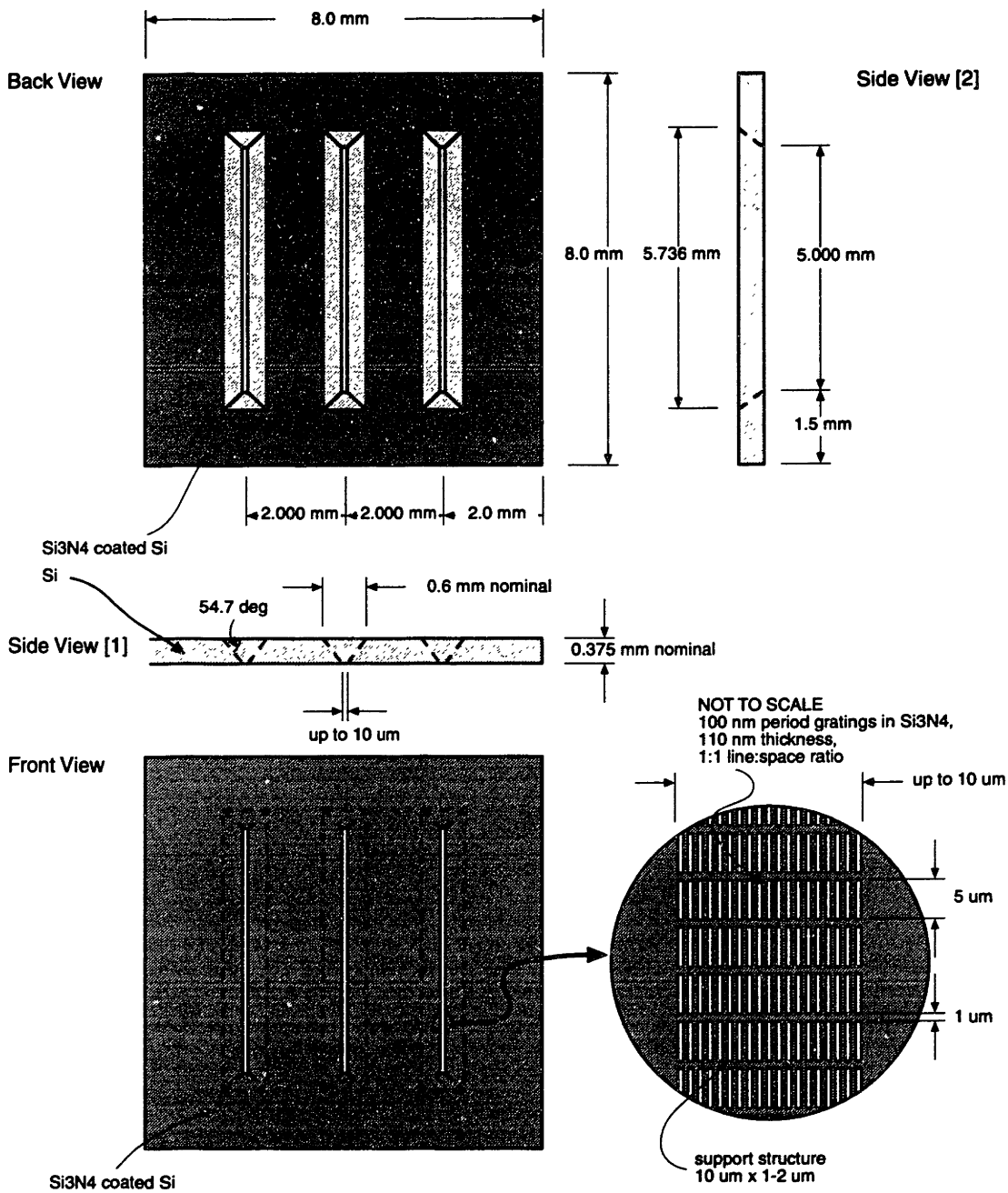

Figure 5-1: Design of $100nm$ period free-standing gratings. The 54.7^o angle present in the platelet is characteristic of the KOH etch process necessary for etching through the silicon substrate.

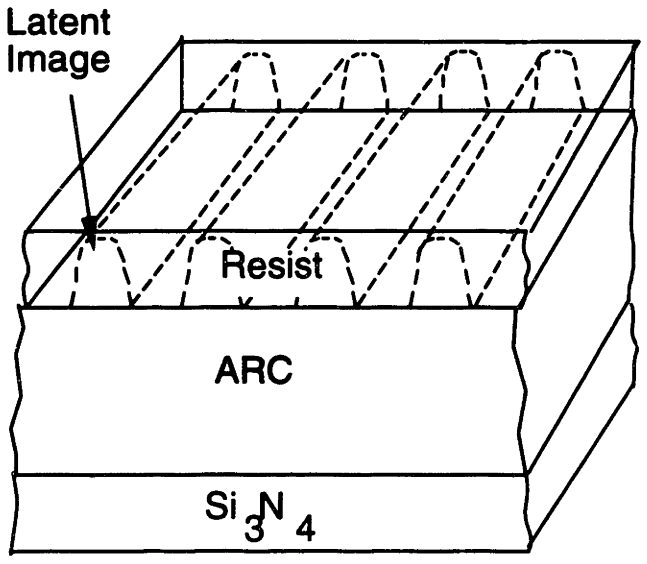

Figure 5-2: Grating exposure.

of anti-reflection coating (ARC) and 1400Å of PMMA. This resist layer is slightly thicker than A. Yen's. Before spin-coating with PMMA, one must cross-link the ARC with a dose of $20J/cm^2$ of $\lambda = 260nm$ radiation, and then anneal the ARC for 30 minutes at 160^oC. Baking time for the PMMA is 1 hour at 180^oC.

The next step is exposure by AHL. Since the exposure time varies with the separation of the motor stops and the portion of the parent grating being imaged, one should perturb the setup as little as possible between monitor runs. Figure 5-2 portrays the exposure.

5.3 Support Structure

Perpendicular to the $100nm$ period free-standing gratings are support structures with a $5.0\mu m$ period and a line:space ratio of 4:1. Before developing the the latent image of the holography, one must transfer the support structure into the resist using UV ($\lambda = 220nm$) lithography (Figure 5-3). Because the features of the support structure mask are so small, one must maintain a good vacuum contact between the mask and the substrate.

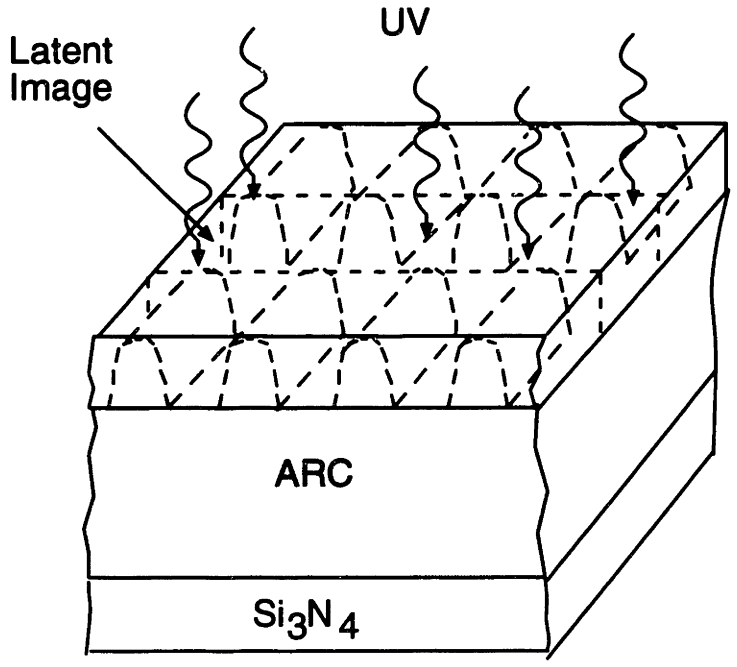

Figure 5-3: Support structure exposure.

5.4 Reactive Ion Etch

The next step is a reactive ion etch to transfer the pattern in the PMMA into the ARC and nitride. The reactive gas for etching ARC is O_2, which also etches PMMA. Therefore, before the etching step, one must protect the the PMMA gratings lines with a protective etch mask. In this case, a shadow evaporator forms titanium caps on the grating lines. The shadow angle must be shallow enough so as not to metalize the grating spaces. Figure 5-4 depicts this process. I viewed monitors in an SEM to determine the height and width of the grating lines in order to determine the best evaporation angle for the desired 1:1 line:space ratio. Currently, the technology lacks precise line:space control, so shadow angles in the $50 - 60^o$ range work equally well.

The O_2 etch lasts for 1 minute, 40 seconds at a power setting of 180 watts. This setting typically corresponds to a bias voltage of about 300 volts (though the voltage tends to be higher when the equipment needs cleaning). ARC tends to heat up and soften during the RIE process, so in order to prevent overheating of the ARC, one must use helium backside cooling to chill the wafer to -30^oC. One must go through several monitors to ensure that the ARC is completely cleaned out of the spaces and that the desired line:space ratio is

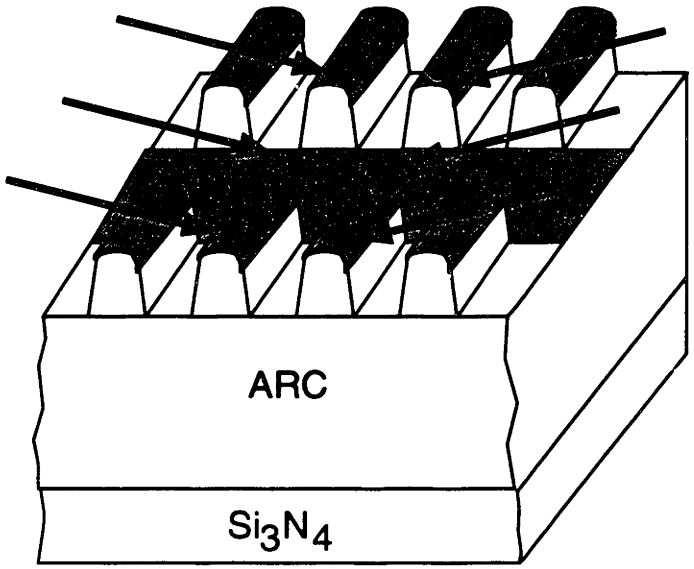

Figure 5-4: Shadow-evaporated titanium protects grating lines and support structures from upcoming reactive ion etch.

masked on the nitride. Timing is important in this step because the etch must completely clean the ARC out of the spaces down to the surface of the nitride. At the same time, if the etch runs for too long, the lines become undercut and gratings lines will tend to fall over. Figure 5-5 shows the the profile of the gratings after this process.

The reactive gas for etching silicon nitride is CF_4. This step follows immediately after the O_2 etch step without exposing the wafer to room temperature. The goal of this step is to etch through the nitride until there is just enough left to survive the wet KOH etch. For 1100Å of nitride, at 180 watts power, etch time is about 2 minutes to etch through 75% of the nitride. I have established that keeping 25% of the nitride layer is sufficient but not necessary for the gratings to survive the silicon etch step. Since the final etch step is the most delicate, it may be wise to do a more aggresive etch now.

After the CF_4 etch step, the profile will look like Figure 5-6. Before proceeding to the next step, one must remove the remaining ARC, PMMA, and Ti using either a piranha or RCA clean.

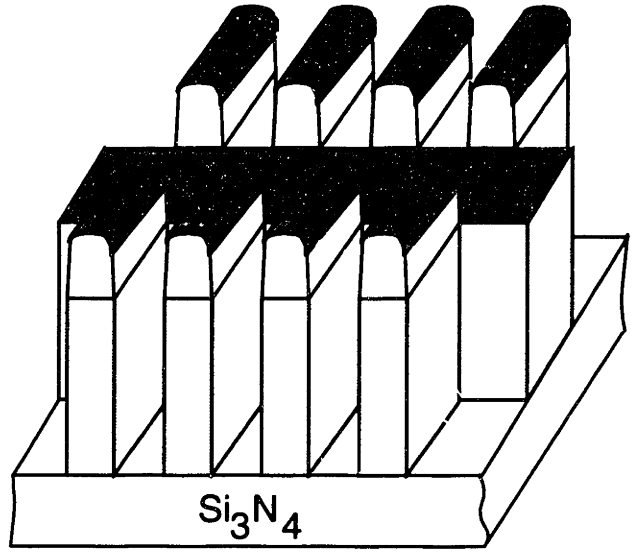

Figure 5-5: Profile of gratings after ARC etch.

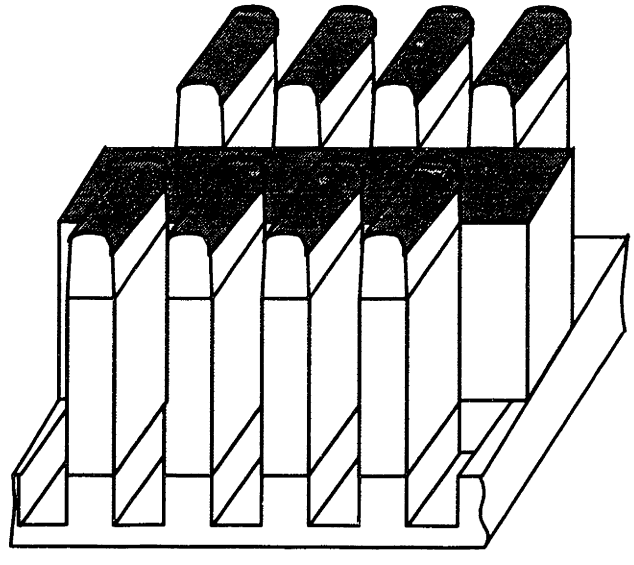

Figure 5-6: Profile of the gratings after partial Si_3N_4 etch. After the etch, enough nitride must remain in the grating spaces to hold the membrane together after the next wet etch step.

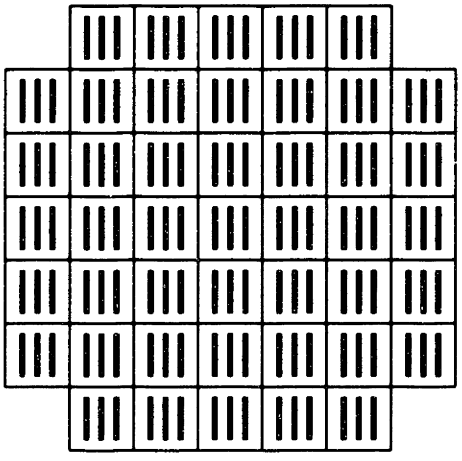

Figure 5-7: Mask containing platelets with variable window sizes. One must experimentally find the best platelet on the mask, and then etch the platelet behind the grating.

5.5 Substrate etch

The next step is to etch the thick silicon substrate away to form membranes. The desired dimensions of the free-standing membranes is at least $10\mu m$ wide by $5mm$ tall. This poses a challenge since we wish to make the membrane as narrow as possible to decrease the likelihood it will break during processing.

J. Lew's thesis describes a method of determining the size of the window corresponding to the desired membrane size. This method requires measuring the thickness of the wafer, however, in order to accurately achieve a $10\mu m$ membrane, one must know the thickness of the wafer within a few microns.

Since it is unrealistic to measure the thickness of a wafer to within such small tolerances, one must use an experimental approach to find the optimal window thickness and etch time. The mask in Figure 5-7 contains outlines of several platelets with windows of varying widths. Using this mask, one etches a monitor wafer and selects the platelet with the optimal window size. For my box of wafers I used $725\mu m$ by $6.5mm$ windows and $200\mu m$ wide cleave lines.

The etch mask for transfering the platelet design into the nitride is 5000Å of Shipley 1813 resist. One must also spin-coat resist on the front side of the wafer to protect it from scratches. One can pattern the back side of the wafers either before or after processing $100nm$ period gratings on the front side, although it seems aligning the platelets afterwards allows one to better line up the platelets on the back to the gratings on the front.

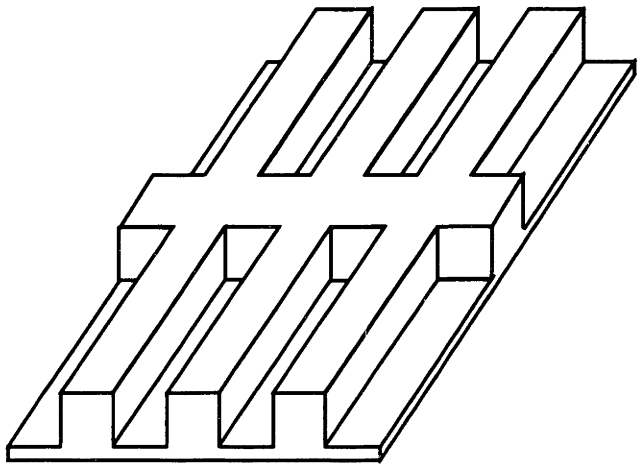

Figure 5-8: Profile of the nitride gratings after the KOH etch. The areas behind the platelet windows are now thin membranes suspended in air.

The KOH takes about 9 hours to etch through the silicon substrate. Since the desired membrane width is so small, one must continuously pull samples out of the etch and examine them under a microscope. Figure 5-8 shows the ideal profile of the gratings after the wet etch step.

5.6 Final RIE

The final step is etching the remaining silicon nitride from the back of the membranes using another CF_4 RIE process. Again, exact timing is critical in this stage. If the etch is too long, the grating lines become weak, but an etch too short will result in gratings that are not free-standing. I etched the nitride membranes for a total time of 2 minutes. To avoid overheating and the consequent destruction of the grating lines, the etch must have low power (50 watts/100 volts) in lieu of backside cooling. After this final step, the gratings will hopefully resemble Figure 5-9.

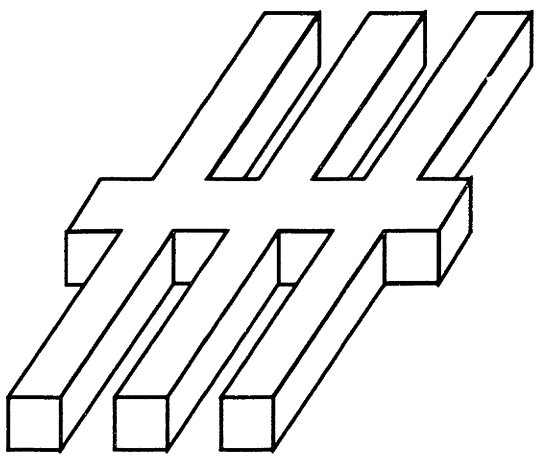

Figure 5-9: Free-standing gratings after the final RIE step.

Chapter 6

Results

After several iterations through the process, I was unable to produce a sample which is free-standing over a large area. Final SEM inspection reveals small areas of free-standing gratings such as in Figure 6-1, but most of the area does not survive the final RIE step.

One clear problem with Figure 6-1 is the thinning of the grating lines where they meet the support structure. The cause for this is the leakage of UV light at the edges of the support structures. This additional light biases the holographic exposure and this decreases the linewidth.

A potential solution to this problem would be using a contact photomask layer over the PMMA. In this scenario one spin-coats a layer of resist (such as AZ photoresist) on top of the PMMA and patterns it with the support structrure. The photomask is opaque to the excimer laser beam and protects the support structures from initial exposure. This technique would yield grating lines that thicken at their ends rather than thin (Figure refprocess.shadow2).

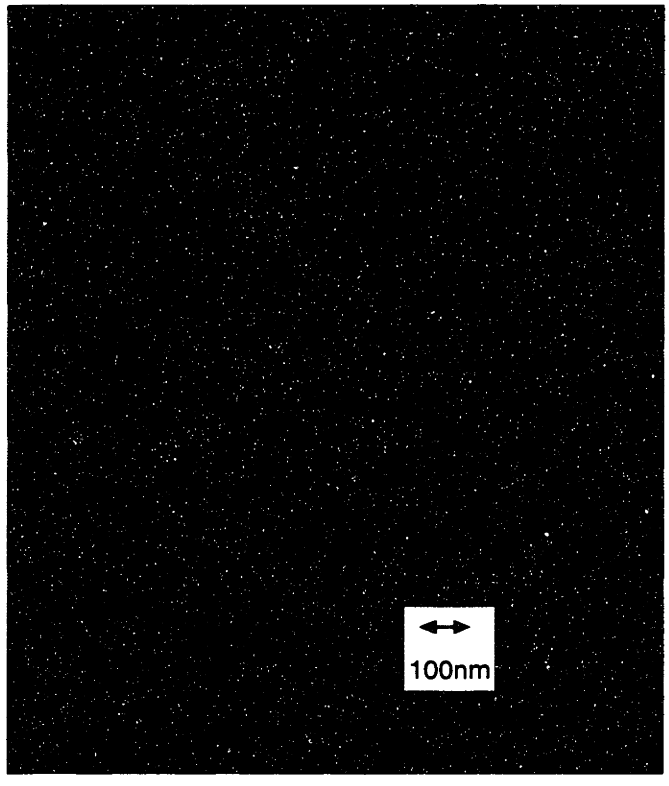

Figure 6-1: 100 nm period free-standing gratings over a small area.

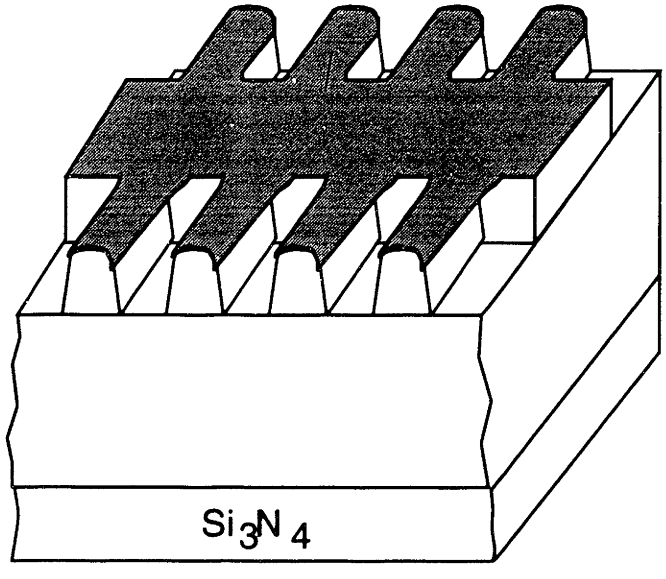

Figure 6-2: If the support structure areas could remain unexposed, the grating lines will thicken towards their ends rather than thin, resulting in stronger structures.

Appendix A

Proof of white-light interferometer

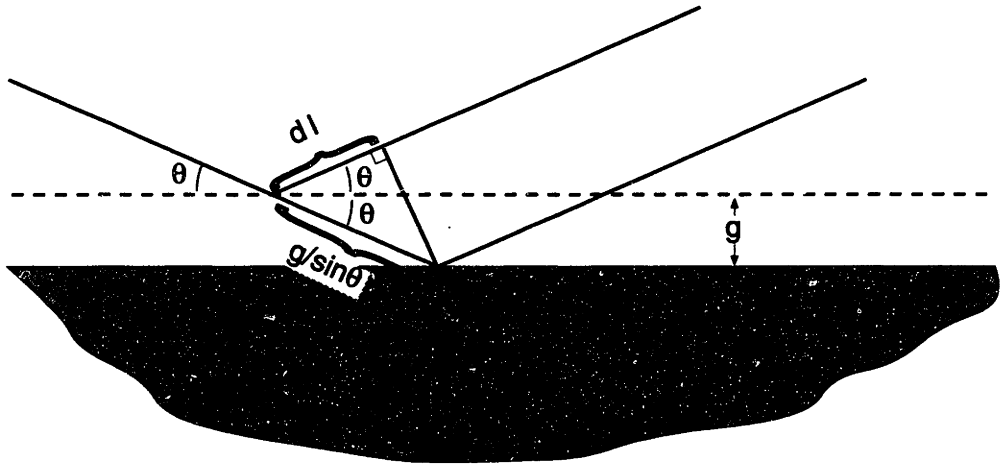

The following is the proof of the sensitivity of the interferometer in Chapter 2. The diagram shows the two white-light paths reflecting at angle θ off a substrate displaced by g. We seek an expression relating g, θ, and the difference in path lengths of the two reflected beams. From the diagram

$$\cos 2\theta = \frac{dl}{g/\sin\theta} \tag{A.1}$$

or

$$dl = \frac{\cos 2\theta}{\sin\theta} g \tag{A.2}$$

Of interest is the path-length difference, given by pld

$$pld = \frac{g}{\sin\theta} - dl \tag{A.3}$$

$$pld = \frac{g}{\sin\theta} - \frac{\cos 2\theta}{\sin\theta} g \tag{A.4}$$

$$pld = g\left(\frac{1-\cos 2\theta}{\sin\theta}\right) \tag{A.5}$$

$$pld = 2g\sin\theta \tag{A.6}$$

Therefore, the change in optical path length is greatest when θ is $\pi/2$, i.e. the light beam is at normal incidence. For light with wavelength λ

$$g = \frac{\lambda}{2\sin\theta} \tag{A.7}$$

is the displacement g corresponding to a single fringe shift in the interferometer.

Bibliography

[1] P. Toennies. Nondestructive mass selection of small van der waals clusters. *Science*, November 25, 1994.

[2] A. Yen. *Fabrication of Large-Area 100 nm-Period Gratings Using Achromatic Holographic Lithography.* PhD thesis, MIT, 1991.

[3] S. Shah. *A White-Light Interferometer for Improved Achromatic Holographic Lithography.* S.B. Thesis, MIT, 1993.

[4] J. C. Lew. *Fabrication of Free-Standing Silicon Nitride Gratings of 200 nm Period for Atom Interferometry.* S.B. Thesis, MIT, 1993.

[5] J. M. Carter, D. B. Olster, M. L. Schattenburg, and Henry I. Smith. Large-area free-standing gratings for atom-interferometry produced using holographic lithography. *Journal of Vacuum Science and Technology*, November/December, 1992.

[6] Physik Instrumente Corporation, Germany.

[7] Velmex Inc., East Bloomfield, NY.

[8] Ace Wheelworks, Somerville, MA.

[9] Acton Research Corporation, Acton, MA.

[10] Frinton Laboratories, Vineland, NJ.

[11] Microlithography Chemical Corporation, Watertown, MA.

THESIS PROCESSING SLIP

FIXED FIELD: ill _____ name _____

index _____ biblio _____

▶ COPIES (Archives) Aero Dewey (Eng) Hum

Lindgren Music Rotch Science

TITLE VARIES ▶☒ "Made" in degree book should be "produced"

NAME VARIES: ▶☐ _____

IMPRINT. (COPYRIGHT) _____

▶ COLLATION: 44 l

▶ ADD. DEGREE: _____ ▶ DEPT.: _____

SUPERVISORS: _____

NOTES:

cat'r: date:

page: F42

▶ DEPT: E.E.

▶ YEAR: 1995 ▶ DEGREE: M.Eng

▶ NAME: SHAH, Satyen N.